Two-fluids RANS predictions of gas cavities, power consumption, mixing time and oxygen transfer rate in an aerated fermenter scale-down stirred with multiple impellers

Two-Fluids RANS predictions of gas cavities, power consumption, mixing time and oxygen transfer rate in an aerated fermenter scale-down stirred with multiple impellers

Francesco Maluta[1]*, Alessandro Paglianti[2], Giuseppina Montante[1]

[1]Dipartimento di Chimica Industriale 'Toso Montanari', Alma Mater Studiorum – Università di Bologna, via Terracini 34, 40131, Bologna, Italy

[2]Dipartimento di Ingegneria Civile, Chimica, Ambientale e dei Materiali, Alma Mater Studiorum – Università di Bologna, via Terracini 34, 40131, Bologna, Italy

** Corresponding author: francesco.maluta2@unibo.it*

The production rate of fed-batch aerobic fermenters is often limited by the oxygen transfer rate that depends on the fluid dynamics of the gas-liquid system. In turn, ideal flow regimes with homogenous distribution of the gas bubbles in the stirred fermenter are not viable, especially at large scale, due huge power requirement at increasing impeller speeds. In this work, a typical flow condition adopted in industrial multiple impeller fermenters is investigated, that leads to gas accumulation on the rear of flat blades, a reduction of the power transferred to the fluid and limitations of the volumetric mass transfer coefficient. Such fluid dynamics features, that are challenging to obtain by fully predictive methods, are well predicted by a Reynolds Averaged Two-Fluid Model and a suitable set of closure equations. The computational method is validated by experimental gas hold-up, gassed power consumption and mixing time data purposely collected in an aerated tank stirred with four Rushton Turbines. The importance of the drag and turbulent dispersion forces magnitude is discussed. The calculated distribution of the oxygen transfer rate highlights the effectiveness of the simulation method as a tool for overcoming mass transfer limitations, which are often a critical step towards the fermentation intensification.

Keywords: CFD, multiple impeller stirred tanks, gas cavity, power consumption, liquid mixing time, oxygen transfer rate

1 Introduction

As process intensification (PI) became an explicit drive to transform chemical and process engineering, it brought a growing ambition to reconsider chemical processes to obtain safer, greener and more energy-efficient plants [1]. Van Gerven and Stankiewicz [2] identified in spatial (to maximize homogeneity), thermodynamic (to maximize driving forces and transfer area), functional (to maximize the synergies), and temporal (to maximize the speed and effectiveness) domains four approaches that realize the goals of PI. While PI pushes for a paradigm shift in the chemical engineering field, the challenges to be faced in most chemical processes are still often mainly related to heat, mass and momentum transfer [3].

Noorman et al. [4] proved that the four approaches of PI are directly applicable to bioprocesses, and especially to industrial fermentations, with additional challenges with respect to chemical processes, since the design space is constrained by the necessity to use mild operating conditions not to damage the microorganisms. In addition, large concentration and temperature gradients and fluctuations can change the cell metabolism [5–7] possibly resulting in reduced productivity. Concentration and temperature gradients and fluctuations may arise just as a result of a change of dimensions of the equipment, since in small size equipment the transport paths are usually short, whereas increasing the scale, the transport rates become the limiting steps controlling the overall rates of reaction [8,9]. As a result, at laboratory scale the fluid flow and reaction regimes are likely not the same as in the large scale [4], hence the optimum operating conditions identified in the lab

are not directly translatable to the production scale [9]. An alternative to the traditional scale-up approach has been identified in the scale-down of industrial equipment, in which the key objective is to maintain similarity between different scales, investigating the main features of the large-scale equipment in a lab-scale system rather than trying to transfer the optimal conditions from the small to the large scale [9–12].

This work is aimed at contributing to the challenging objective of devising a fully predictive Computational Fluid Dynamics (CFD) method for the description of large scale equipment, which can be used to design scale-down fermenter set-up and operation conditions, as suggested by Noorman and Heijnen [9]. Due to the large sizes typically adopted in industrial equipment, an accurate description of the smaller scales of the flow and of its turbulent variables is not possible, since their description would require very fine spatial and temporal discretization leading to prohibitively long simulation times. Industrially feasible modelling approaches, based on the solution of Reynolds Averaged Navier-Stokes (RANS) equations, are needed for maintaining affordable computational requirements. In addition, at industrial scale the grid independency of the predictions must be renounced, since the turbulent variables would require a huge number of computational cells [13].

The focus of this investigation is on the variables that affect fed-batch large-scale industrial fermenters the most. In these fermenters the maximum production rate is determined by limiting transport processes, among which the most relevant for aerobic fermentation are the oxygen supply and the liquid mixing of compounds added from the inlet into the bioreactor volume [4]. The prediction of the liquid mixing time and the oxygen transfer rate is strongly related to the prediction of fundamental two-phase flow variables and specific hydrodynamics features of gas-liquid stirred tanks, such as the gas accumulation at the rear of the impeller blades [14], the consequent drop of

power consumption that affects the volumetric mass transfer coefficients [15], the local turbulent variables that influence the bubble size distribution [16] and the mixing time.

The investigation is applied to the typical industrial fermenter geometry, that is a tank stirred with multiple Rushton impellers, in which the lowest impeller works in the loading flow regime. It corresponds to a non-ideal flow, since the bubbles are not recirculated below the lowest impeller, but a good balance between performance and cost is usually obtained, while not posing serious limitations to mass transfer [4]. In multiple impeller stirred tanks achieving homogeneous dispersion conditions and having all the impellers working in the same flow regime may result in unaffordable operating costs [4]. The capability to predict the flow regimes in multiple impeller stirred tanks accounting for the real geometry and size is paramount in the analysis of the fermenter performances. Gas accumulation behind the blades of the impeller, which is typically observed in Rushton turbines, significantly reduces the pumping efficiency and the power transferred from the impeller to the fluid [14,17]. The strong difference between the impeller region and the rest of the multiple impeller stirred tank volume and the consequent power reduction in gas-liquid systems poses significant simulation challenges similarly to the case of multiple impeller stirred tanks containing yield stress fluids [18,19].

Despite the importance of the gas cavities in industrial fermentation and fermentation intensification, few numerical studies have addressed the topic [20–27] and the gas accumulation behind the impeller blades was generally underestimated since it was either not predicted (e.g. [25]) or only partially predicted (e.g. [27]), being generally the gas volume fractions at the rear of the blades lower than 0.5 instead of nearly 1, as observed in the experiments.

Single impeller gas-liquid stirred tanks have been extensively studied in the literature, considering several aspects and leading to different modelling alternatives in the Two-Fluid Model (TFM)

framework, going from a detailed analysis of the turbulent fluid flow features [28,29], to the prediction of the bubble size and the local gas volumetric fraction distributions [26,30], the liquid mixing time [31] and the gas-liquid mass transfer [32]. Recently Shi and Rzehak [29] have presented a short review of the most relevant experimental and computational results highlighting the need for more comprehensive data for model validation. Less attention has been comparatively devoted to the numerical analysis of multiple impeller gas-liquid stirred tanks. Some of the first publications were mostly focused on the prediction of the flow regimes at different gas flow rates, the effect of the local flow patterns on mixing conditions [33,34], gas dispersion and bubble size [23]. The prediction of the cavities behind the impeller blades is generally somewhat incomplete, since an accumulation of gas was correctly predicted by different models, but the local volume fraction is generally much lower than 1, e.g. the results of Kerdousse et al. [23] did not exceed ~0.1, while Khopkar & Tanguy [33] predicted the gas accumulation behind the impeller blades up to a gas volume fraction of ~0.3. To obtain a reduced power consumption as observed in the experiments, Taghavi et al. [35] implemented an empirical correlation with an adjustable parameter, based on the work by Fajner et al. [36], but it is not clear whether the power reduction is due to the increased overall gas hold-up or due to the formation of cavities. Dual Rushton impeller tanks were also studied by Ahmed et al. [37] mostly focusing on the prediction of the power consumption, by Liu et al. [38] in order to predict the shear forces in the reactor, by Wang et al. [39] directing attention on the gas hold-up at low gas flow regimes, by Teli et al. [40] in a study concerning different impeller speeds and by Gakingo et al. [41] in a study concerning a three-phase system.

Overall, in the RANS simulation based on the Two-Fluid Model, the predictions of key parameters for industrial fermenter design, that are the gas hold-up, power consumption and mixing time

depend on the closure models required for the description of the momentum and the turbulent transfer between phases. A well-established set of models for obtaining reliable results of different aspects has not been identified so far. In the following, a methodology for the viable simulation of fermenter of any scale for capturing the above-mentioned key features without the adoption of adjustable parameters is presented and its overall reliability is demonstrated by comparison of the prediction of some of the most important variables for fermentation with novel experimental data and previous literature results.

2 Experimental

The experimental cylindrical, flat-bottomed tank stirred by four identical Rushton impellers mounted on the same axial shaft had the typical geometrical characteristics of a laboratory scale aerobic fermenter. The tank had a diameter, *T*, of 0.23m and it was equipped with four equally spaced baffles of width equal to *T*/10. The impellers had a diameter, *D*, equal to *T*/3, the lowest impeller had an off-bottom clearance equal to *T*/2 and the distance between two consecutive impellers was equal to *T*. The liquid volume reached the total height, *H*, of 4*T*, thus the vessel consisted of four equal standard geometry stirred tanks of height *T* (referred to as stages) and the corresponding Rushton impeller was positioned at a relative height of *T/2*. Below the lowest impeller, at an off-bottom axial distance of *T/5*, a ring sparger of diameter *0.4D* was positioned.

Air (density $\rho_G = 1.2$ kg/m^3) was injected in demineralized water at room condition (density $\rho_L = 998$ kg/m^3 and viscosity $\mu_L = 0.001$ Pa·s,) from the sparger at a flow rate, Q, of 250 L/h, corresponding to a superficial gas velocity of 1.67×10^{-3} m/s and to a volumetric aeration rate of 0.11 vvm. The impeller rotational speed, *N*, of 5 s^{-1}, was selected for agitation, for achieving a gas-liquid condition similar to that often adopted in industrial fermentation, corresponding to a gas flow number, $Fl_g=Q/D^3 N$, equal to 0.03 for the lowest impeller. Turbulent flow conditions were

achieved for the liquid phase, since the rotational Reynolds number, based on the liquid physical properties, $Re = ND^2\rho_L/\mu_L$, was equal to 2.9×10^4. For this conditions, an average gas hold-up of 1.15×10^{-2}, a gassed power number, $Np_g = P_g/\rho_L N^3 D^5$, of 15.7 with P_g being the gassed power consumption, and a liquid mixing time, t_{90}, of 68s, defined as the time needed to reach the 90% degree of homogeneity were measured. The ungassed power number, $Np_u = P_u/\rho_L N^3 D^5$, in the same system was equal to 18.5, with P_u being the ungassed power consumption. The gas hold-up was obtained by measuring the level drop after agitation and gas supply were switched off. The power number was estimated from the power input measured from the torque necessary to prevent the rotation of the motor, which was suspended from its top. The mixing time was obtained from the measurement of the time evolution of liquid conductivity at the top of the vessel, after the very rapid injection of a saturated aqueous solution of KCl from the bottom.

Based on the visual observation of the experimental system and supported by the literature correlations of Nienow et al. [42] and Warmoeskerken and Smith [14], large cavities are present behind the blades of the lowest impeller, which works under the loading regime. For a quantitative analysis, the area of the gas cavities formed at the rear of the blades measured by of Paglianti et al. [43] by an image analysis technique in a single-impeller stirred tank is also considered.

3 Model description

The simulations concerned the same gas–liquid stirred tank experimentally investigated. The modelling was based on the standard formulation of the Two-Fluid model equations, namely the Eulerian multifluid model as implemented in ANSYS Fluent 19.3. Based on the operating conditions defined in the previous section, the steady state, incompressible, isothermal, Reynolds

averaged continuity and momentum conservation equations of each fluid were selected, that read as:

$$\nabla \cdot (\alpha_i \rho_i \boldsymbol{u_i}) = 0 \quad (1)$$

$$\nabla \cdot (\alpha_i \rho_i \boldsymbol{u_i u_i}) = -\alpha_i \nabla P + \alpha_i \rho_i \boldsymbol{g} + \nabla \cdot (\boldsymbol{\tau_i} + \boldsymbol{\tau_i^t}) + \boldsymbol{F_D} + \boldsymbol{F_{TD}} \quad (2)$$

Where α_i is the volume fraction of the phase i, ρ_i is its density, $\boldsymbol{u_i}$ is the mean velocity vector of the phase i, $\boldsymbol{\tau_i}$ and $\boldsymbol{\tau_i^t}$ are its laminar viscous stress tensor and the Reynolds stress tensor respectively, P is the pressure and $\boldsymbol{g}$ is the gravitational acceleration. The liquid and gas momentum equations are coupled through two interphase momentum exchange terms: the interphase drag force, $\boldsymbol{F_D}$, and the turbulent dispersion force, $\boldsymbol{F_{TD}}$. Additional interphase momentum exchange forces, namely lift, added mass and wall lubrication are not included, having found their contribution being always negligible in previous investigations concerning gas-liquid stirred tanks (e.g. [22,30]).

The Reynolds stress tensor was obtained with the standard $k - \varepsilon$ turbulence model extended to multiphase flows, as implemented in the ANSYS Fluent 19.3 CFD software with three different approximations [44], *i.e.* considering phase-averaged properties (mixture formulation), just the continuous phase properties and using simplified relationships for the dispersed phase turbulence based on the Tchen theory of dispersion of discrete particles by homogeneous turbulence (dispersed formulation) or solving two sets of differential equations, one for each phase (per phase formulation).

The interphase drag force for spherical bubbles of diameter d_B is defined as:

$$\boldsymbol{F_D} = \frac{3}{4}\frac{\alpha_G}{d_B} C_D \rho_L \|\boldsymbol{u_G} - \boldsymbol{u_L}\|(\boldsymbol{u_G} - \boldsymbol{u_L}) \quad (3)$$

With $\boldsymbol{u_G}$ and $\boldsymbol{u_L}$ being the gas and liquid averaged velocities respectively and C_D being the drag coefficient.

The turbulent dispersion force was modelled as Burns et al. [45]:

$$\boldsymbol{F_{TD}} = \frac{3}{4}\frac{\alpha_G}{d_B} C_D \rho_L \|\boldsymbol{u_G} - \boldsymbol{u_L}\| \left[\frac{\mu_t}{\rho_L Sc_{t,L}}\left(\frac{\nabla \alpha_G}{\alpha_G} - \frac{\nabla \alpha_L}{\alpha_L}\right)\right] \quad 4$$

With μ_t being the turbulent viscosity and $Sc_{t,L}$ the turbulent Schmidt number for the liquid phase that has the default value of 0.9.

To obtain the drag coefficient, the Grace et al. [46] model was used, that considers different correlations depending on the bubble shapes. In the operating conditions studied in this work, just two different bubble shapes can be found, namely spheres and ellipses. The drag coefficient is obtained as follow:

$$C_D = \alpha_L^{C^{exp}} max\left(C_{D,ellipse}, C_{D,sphere}\right) \quad 5$$

Where C^{exp} is a correction exponent for the liquid volume fraction. In case of spherical particles, $C_{D,sphere}$ is calculated with the well-known Schiller and Nauman correlation [47], as:

$$C_{D,sphere} = \frac{24}{Re}\left(1 + 0.15 {Re_p}^{0.687}\right) \quad 6$$

That holds true for isolated rigid spheres falling in still fluids in the following range of particle Reynolds number, $0.1 < Re_p < 1000$, with $Re_p = \|\boldsymbol{u_G} - \boldsymbol{u_L}\| d_B \rho_L / \mu_L$.

In case of elliptical shape, $C_{D,ellipse}$ is estimated from the bubble terminal velocity, calculated as:

$$U_{t,ellipse} = \frac{\mu_L}{\rho_L d_B} Mo^{-0.149}\left(C_1\left[\frac{4}{3} EoMo^{-0.149}\right]^{\beta} - 0.857\right) \quad 7$$

Where the Morton number is $Mo = \mu_L^4 \boldsymbol{g}(\rho_L - \rho_G)/(\rho_L^2 \sigma^3)$, and the Eötvös number is $Eo = \boldsymbol{g}(\rho_L - \rho_G) d_B^2/\sigma$, with σ being the water surface tension equal to 0.072 N/m. C_1 and β are equal to 0.94 and 0.757 respectively, when the term in square brackets is between 2 and 59.3, and C_1 and β equal to 3.42 and 0.441 respectively, when the term in square brackets is bigger than 59.3.

The drag coefficient and the terminal velocity relationship for the elliptical bubbles is obtained from the force balance on the single bubble in the vertical direction:

$$C_{D,ellipse} = \frac{4}{3} \frac{\boldsymbol{g} d_B}{U_{t,ellipse}^2} \frac{(\rho_L - \rho_G)}{\rho_L} \qquad 8$$

C^{exp} is taken equal to 0 or 1 in this work, in order to investigate the effect of the drag coefficient on the predictions. It is worth observing that both values have been adopted in previous works, leading to either considering the drag force linearly dependent on α_G (e.g. [25,28]) only or on $\alpha_G \times \alpha_L$ (e.g. [20,22]). Generally, many correlations for the drag coefficient and possible corrections due to different effects (high volume fraction, free stream turbulence, surface active components) have allowed to obtain good predictions of different variables without achieving conclusive results.

Besides, it is also useful to recall that, as already reported by Scargiali et al. [25], when the terminal velocity is employed to express the interphase drag force, any reference to particle diameter, projected area or volume disappears from the drag force formulation. Based on these considerations and adopting Eq. 5, Eq. 3 becomes:

$$\boldsymbol{F_D} = \alpha_L^{C^{exp}} \frac{\alpha_G}{U_t^2} \boldsymbol{g}(\rho_L - \rho_G) \|\boldsymbol{u_G} - \boldsymbol{u_L}\| (\boldsymbol{u_G} - \boldsymbol{u_L}) \qquad 9$$

This observation makes the adoption of the Grace correlation particularly suitable for the implementation into the drag force formulation also in case of elliptical bubbles.

3.1 The bubble size modelling

In the Two Fluid Model framework, the bubble size is considered just in the interphase forces formulations. The size distribution of the bubbles can be accounted for by different approaches, with the simplest being the adoption of a delta distribution of the bubble size, i.e. constant diameter. Besides the obvious advantages of computational cheapness with respect to polydisperse modelling methods, this assumption proved to be reasonable for industrial fermenters, since the presence of surface-active additives prevents coalescence phenomena, thus leading to relative narrow bubble size distributions [4,48–50]. For these reasons, a constant diameter was assumed in this study, based on correlations for bubble size in the bulk, $\overline{d_B}$, of non-coalescing (Eq.10) and coalescing (Eq.11) systems by Alves et al. [51]

$$\overline{d_B} = 0.014 \left(\frac{P_g}{V}\right)^{-0.37} \quad (10)$$

$$\overline{d_B} = 0.0076 \left(\frac{P_g}{V}\right)^{-0.14} \quad (11)$$

In Eq. 10 and Eq. 11, P_g is the aerated power consumed by the impellers and V is the liquid volume. For the investigated operating conditions, based on the experimental aerated power consumption, bubble diameters equal to 2.3 mm and 3.8 mm were obtained for non-coalescing and coalescing systems, respectively. Similar values were obtained with the correlations for the maximum stable diameter, modified by Wang et al. [52] and Zhang et al. [53] to obtain the Sauter mean diameter for air/water dispersions. Diameters lower than those predicted by the correlations for the bulk bubble size by Alves et al. [51] were also considered since smaller diameters might be expected in the proximity of the impeller blades. Finally, bubble diameters from 1mm to 4mm were assumed in the simulations.

According to the Grace model [46], in the operating conditions considered, 1mm diameter bubbles behave as rigid spheres, whereas an ellipsoidal shape is obtained with bubble diameters of 2mm, 3mm and 4mm, as shown in Fig.1.

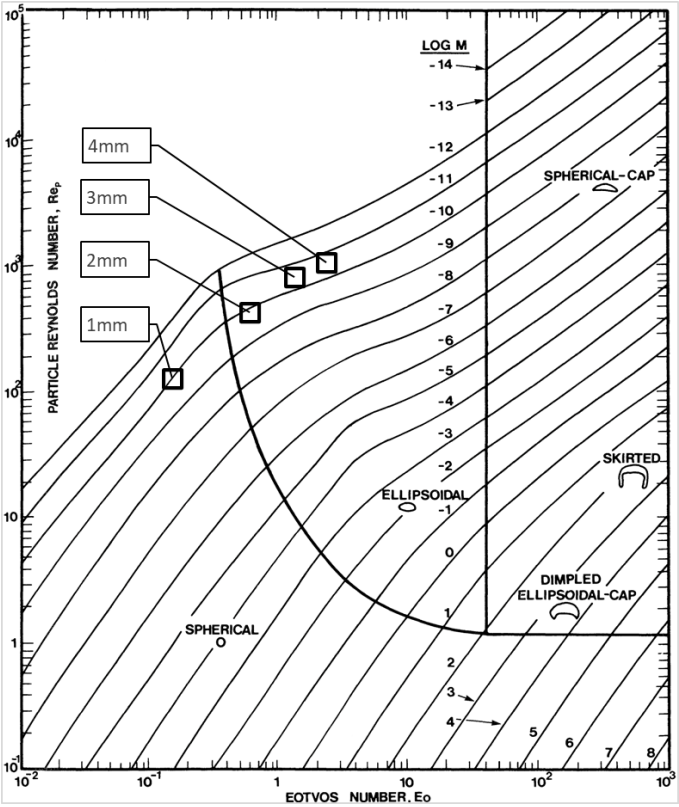

Figure 1 - Shape regimes for bubbles in motion through liquid media. Figure adapted from (Clift, Grace and Weber, 2005 [46]*). The squares represent the shape regimes for the different bubble diameters considered in this work.*

Fig.1 shows the shape regimes for bubbles in unhindered gravitational motion through liquids, as obtained from the adoption of the drag law formulated by Grace. As the bubble diameter increases, the particle Reynolds number and the Eötvös number also increase, resulting in a shift from spherical bubbles to ellipsoidal, that in the condition studied occurs between 1mm and 2mm diameter bubbles. As a result, according to the Grace et al. correlation, the rising velocity of an

isolated bubble of 1 mm in a still fluid is equal to 11cm/s, it almost doubles to 20 cm/s for 2 mm bubbles and much slighter variations are observed with 3mm and 4mm bubbles, that have the same rising velocity of 25 cm/s.

3.2 The liquid mixing time model

The homogenization dynamic of a passive tracer in the liquid phase was obtained by solving a Reynolds-averaged time-dependent scalar transport equation.

$$\frac{\partial \alpha_L \rho_L Y_L^{PT}}{\partial t} + \nabla \cdot (\alpha_L \rho_L Y_L^{PT} u_L) = \nabla \cdot \left(\alpha_L \left(\rho_L D_L^{PT} + {}^{\mu_t}/_{Sc_t} \right) \nabla Y_L^{PT} \right) \quad 12$$

where Y_L^{PT} is the mass fraction of the passive tracer in the liquid phase. The water molecular diffusion coefficient, D_L^{PT}, was assumed equal to 2.6×10^{-9} m^2/s and the turbulent Schmidt number, Sc_t, was equal to 0.7. It is worth mentioning that the governing transport mechanism is convection and turbulent diffusion, while the molecular diffusion contribution is generally negligible. The passive scalar was injected below the lowest impeller at the same location of the experiments and the transport equation was solved in a stationary flow field at the steady state.

3.3 Mass transfer model

The gas-liquid mass transfer was modelled assuming an oxygen concentration of 21% mol in the air stream sparged in the vessel and a constant concentration of dissolved oxygen in the water phase equal to 3mg/L. A convection-diffusion equation for each of the species was solved in order to model the species transport in each phase. The conservation equation for each component assumes the following form:

$$\nabla \cdot \left(\alpha_i \rho_i Y_i^k u_i \right) = \nabla \cdot \left(\alpha_i \left(\rho_i D_i^k + {}^{\mu_t}/_{Sc_t} \right) \nabla Y_i^k \right) + \left(\dot{m}_{ij}^k - \dot{m}_{ji}^k \right) \quad 13$$

With Y_i^k being the mass fraction of the species k in the i-th phase, and $\dot{m}_{ij}^k$ and $\dot{m}_{ji}^k$ being the mass transfer of k from the phase j to the phase i and vice versa, respectively. The diffusion flux is modelled with a modified version of the Fick's law of diffusion, to consider the increased diffusion due to turbulence.

The interphase flux of oxygen, $\dot{m}_{LG}^{O_2}$, also referred to as oxygen transfer rate (OTR), was modelled as:

$$\dot{m}_{LG}^{O_2} = k_L a \rho_i (Y_L^I - Y_L) \quad 14$$

In which the liquid side mass transfer coefficient is indicated as k_L, the specific interfacial area as a and the concentration of the oxygen dissolved in the bulk of the liquid phase as Y_L. The oxygen concentration in the liquid phase at the interface between the gas and the liquid phase, Y_L^I, was obtained from Henry's law:

$$Y_L^I = p^{O_2}/K_H \quad 15$$

Where p^{O_2} is the partial pressure of oxygen in the gas phase and K_H is the Henry's constant equal to 2.5×10^9 Pa. The gas phase was modelled as perfectly mixed, thus assuming negligible species transport resistance in the gas phase.

The liquid side mass transfer coefficient is obtained from the eddy cell model of Lamont and Scott [54], as extensively done in the literature [10,32]:

$$k_L = 0.4 D_L^{0.5} (\varepsilon/\nu)^{0.25} \quad 16$$

With D_L being the oxygen diffusion coefficient in water equal to 2×10^{-9} m^2/s and ν being the liquid kinematic viscosity. As proposed by Maluta et al. [55], the specific interfacial area is obtained as:

$$a = \begin{cases} 6\alpha_G/d_B\,, & \alpha_G \leq 0.3 \\ 4\pi \left(\frac{3}{4\pi}\alpha_G\right)^{2/3}/V_{cell}^{1/3}, & 0.3 < \alpha_G \leq 0.5 \\ 4\pi \left(\frac{3}{4\pi}\alpha_L\right)^{2/3}/V_{cell}^{1/3}\,, & \alpha_G > 0.5 \end{cases} \quad 17$$

In which V_{cell} is the volume of the computational grid cell. Further information on the interphase mass transfer model adopted in this investigation can be found in Maluta et al. [55].

4 Computational domain and solution procedure

The simulations were run in the computational domain shown in Fig. 2, that closely matched the geometry of the stirred tank described in Section 2, discretized in about 900,000 hexahedral cells.

To analyze the spatial discretization effect with reasonable computational times, the numerical domain was reduced to just the first stage (H=T, single Rushton Turbine at z/T =0.5) and in addition to the grid adopted for the multiple impeller case, a new finer grid was obtained by dividing each cell edge of the original mesh into two edges. The resulting number of cells (~2 Million cells) was therefore 8 times the number of cells of the original mesh on a single stage. As expected based on previous investigations on single-phase stirred tanks [13], the mean flow variables were found to be grid independent, while the turbulent variables were not.

To apply the computational method to industrial scale equipment while maintaining the advantages of RANS based simulations, that are adopted as an alternative for other more computational intensive methods (e.g. Large Eddy Simulations, Direct Numerical Simulations), the achievement of grid independent turbulent variables prediction must be renounced. Correction methods may be derived when the underestimation of the turbulent variables due to the coarse grid

effect prevent the realistic prediction of the variables of interest in the investigated process, as proposed by Gao et al. [56] for liquid-liquid stirred tanks.

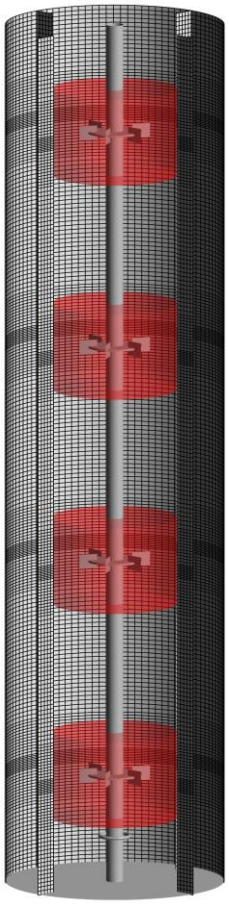

Figure 2. Fermenter meshed geometry. The interfaces between rotating and stationary frames are defined by the red surfaces.

The volume was divided into 5 different domains: one for the cells in the proximity of each impeller, in order to describe the relative motion of the rotating impellers (by using the multiple reference frame, MRF, algorithm) and one for the remaining cells. The boundary conditions at the solid walls were modelled with no-slip conditions for both phases. On the upper surface of the air-sparger a single-phase velocity inlet with velocity equal to 0.69 m/s was assumed for the gas phase, resulting in a flow rate of 250 L/h and on the free surface at the top of the fermenter a degassing

boundary condition was adopted, so that the gas phase can leave the system, but the liquid phase cannot. The second order upwind discretization scheme was used for the momentum equations, the transport of turbulent variables, of the species and of the passive tracer while the QUICK scheme was used for the volume fraction. The pressure-velocity coupling was achieved by means of the pressure-based coupled algorithm as implemented in ANSYS Fluent. The system operated at the steady state in single-phase conditions was used as the initial conditions for the simulations. As for the fluid dynamics simulations, air was then injected from the sparger and the two-phase steady state solution was achieved by means of a pseudo-transient approach [57] with pseudo-time-steps of 0.001s. This approach allows under-relaxed iterative steady state calculation and it was necessary to ensure mass conservation, since steady-state MRF two-phase TFM simulations in Fluent do not enforce that. The iterative solution of the steady state equations was stopped after the scaled residuals reached constant values of the order of 10^{-5} - 10^{-6}. Additional convergence criteria were also considered, ensuring that the forces measured on the baffles and on the impeller blades reached a constant value and that the net mass flux exiting the system equalled the net mass flux injected from the sparger, to achieve accurate mass balance.

As for the mixing time prediction, the accumulation term in the transient passive scalar transport equation was discretized with a second order implicit formulation and the equation was iteratively solved with a time step of 0.1s and 25 inner iterations, that were sufficient to reach a constant value of the scaled residuals in each time step. Convergence was assumed when the passive scalar concentration reached a constant value on the monitoring points defined in several positions of the stirred tanks.

The mass transport model equations were solved in a gas-liquid “fixed” flow-field, in order to reduce the computational time, with the pseudo-transient approach [57] with pseudo-time-steps of

0.001s. Convergence was assumed when the scaled residuals reached constant values of about 10^{-4} – 10^{-5} and when the overall oxygen mass fraction in the gas phase reached a constant value, meaning that the net interphase mass transfer rate achieved the steady state value.

5 Results and discussion

In the operative conditions considered in this work, the lowest Rushton impeller works in the loading regime [42]. Moreover, from experimental visual observations, large gas cavities establish at the rear of the blades of the lowest impeller, consistently with previous literature results [14] and with the measured aerated power consumption reduction with respect to the ungassed condition. The prediction of these hydrodynamics features and their validation by comparison with experimental data will be addressed in the following.

Given the extensive literature proving that for RANS simulations of baffled stirred tanks no advantages are obtained with different models, the $k-\varepsilon$ turbulence model was selected in this work. Preliminary simulations were run to estimate the possible effect of different multiphase $k-\varepsilon$ model formulations (mixture, dispersed, per phase). The comparison is based on results obtained from the solution of the equations presented in Section 3 with the constant bubble diameter of 2mm and C^{exp}=1 in Eq. 5. Negligible differences were observed in the overall gas hold-up, in the gassed power number as obtained from the torque on the four impeller blades, Np_g, and on the liquid phase turbulent dissipation rate integrated in each of the 4 stages of the fermenter, as shown in Tab. 1, where the 1st stage is the lowest (in which the impeller is positioned at z/T =0.5) and the 4th stage is the highest (in which the impeller is positioned at z/T =3.5).

Table 1 – Comparison of selected global variables obtained from different multiphase formulations of $k-\varepsilon$ turbulence model

Two-phase $k-\varepsilon$ turbulence model	Gas hold-up	Np_g	Liquid phase Volume integral of ε – [m^5/s^3]			
			1st stage	2nd stage	3rd stage	4th stage
mixture*	8.6×10^{-3}	14.9	8.7×10^{-4}	9.2×10^{-4}	1.0×10^{-3}	1.0×10^{-3}
dispersed	8.6×10^{-3}	14.8	8.1×10^{-4}	1.0×10^{-3}	1.0×10^{-3}	1.0×10^{-3}
per phase	8.8×10^{-3}	14.1	8.3×10^{-4}	9.4×10^{-4}	1.0×10^{-3}	1.0×10^{-3}

*Liquid phase Volume integral of ε is obtained multiplying the turbulent dissipation rate by the liquid phase volume fraction

Since the turbulence model formulations considered in this work produce very similar results, the mixture formulation of the standard $k-\varepsilon$ turbulence model was used. This formulation proved to be more robust than the others, also resulting in shorter computational times.

5.1 Assessment of the predictions of gas cavities and gassed power consumption by comparison with experimental data

The formation of large gas cavities behind the impeller blades obstructs the passage of liquid through the impeller and it is mostly responsible for the reduction of the effective power number [58]. A thorough and detailed description of the phenomenon can be found in previous works [14,42,59]. In the following the predictions of the gas accumulation and of the power consumption are discussed.

5.1.1 Effect of the bubble size

The gas phase distributions as obtained with the four different bubble diameters, which correspond to different bubble terminal velocities/drag coefficient, and C^{exp}=1 in Eq. 5 are shown in Fig. 3.

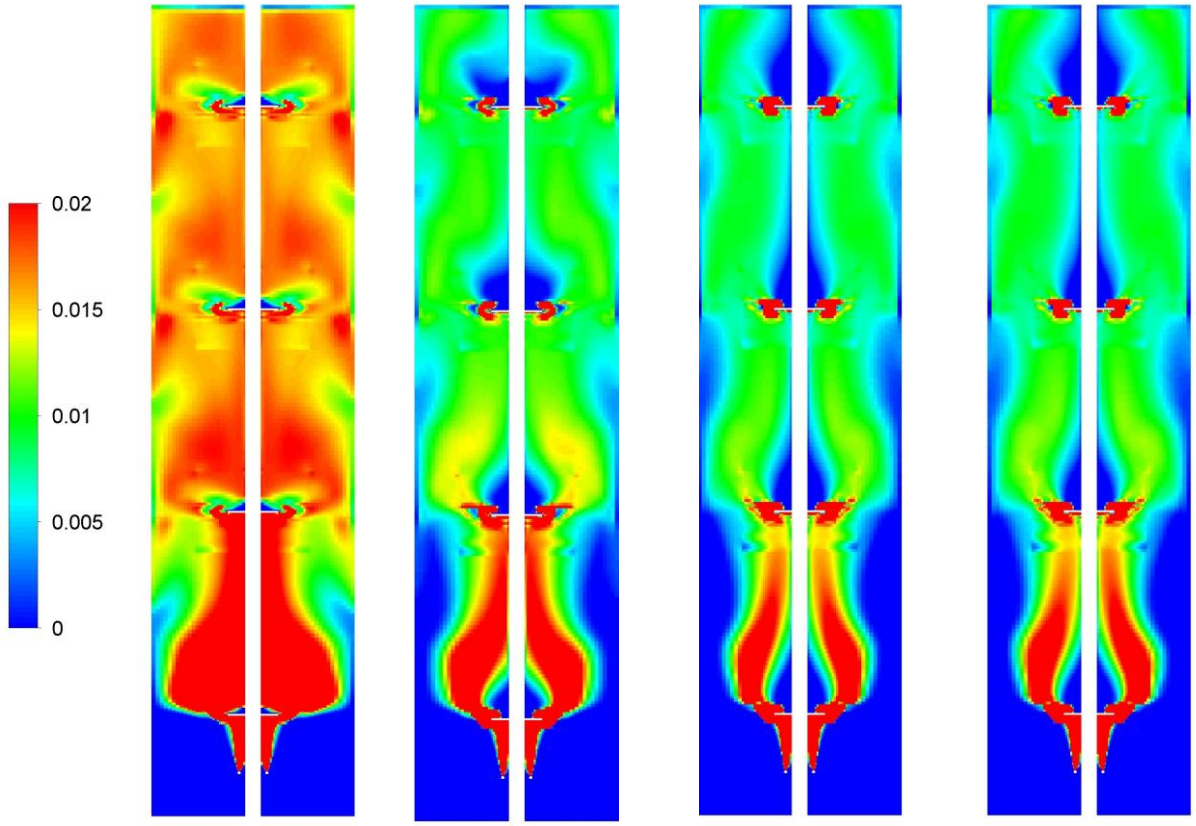

(a) (b) (c) (d)

Figure 3 – Gas volume fraction distribution on a plane midway two consecutive baffles, as predicted by the simulations with constant bubble diameter of 1mm (a), 2mm (b), 3mm (c) and 4mm (d).

Fig. 3 shows that a significantly different gas distribution is obtained doubling the bubble size from 1mm to 2mm, whereas the gas distribution varies slightly moving from 2mm to 3mm bubbles

and almost no difference is obtained considering either 3mm or 4mm bubbles, as expected based on the preliminary calculation of the bubbles rising velocity. In all cases, the lowest impeller works in loading regime, in fact the gas pumped below the plane of the lowest impeller is almost nil with the bubbles of 1mm and nil for the other bubble sizes, while the regime of the three upper impellers passes from recirculation to loading, depending on the bubble size. The overall gas hold-up predicted by the simulations decreases from 1.43% to 0.86% and 0.79%, with bubble diameters of 1mm, 2mm and 3-4mm, respectively. All these results are not far from the experimental gas hold-up of 1.15%. A precise evaluation of the most reliable value is not possible, due to the experimental error associated to the visual determination of the change in liquid level.

A stricter evaluation can be performed considering the gas accumulation at the rear of the impeller blades. In Fig.4, the cells with a gas volume fraction higher than 0.95 in the lowest impeller region are shown. The presence of the gas cavities is apparent for the three cases of bubbles larger than 1mm. In the upper impeller blades (not shown for brevity), the gas accumulation does not occur with the 2 mm bubbles, while large gas cavities were found in the simulations with 3 mm and 4 mm bubbles. Since in the TFM the bubble size is solely adopted for the drag coefficient/bubble terminal velocity calculations, these results confirm the importance of the drag magnitude on the prediction of the main two-phase fluid dynamics features in the TFM context.

The presence of large gas cavities behind the lowest impeller blades results in a reduced power transferred to the mixture equal to Np_g/Np_u = 0.85, as obtained from the experimental ungassed Np_u and gassed Np_g overall power numbers equal to 18.5 and 15.7, respectively. The corresponding predicted values obtained from the torque on the impeller blades are equal to 19.2 for the single phase case and to 17.4, 14.9, 12.5 and 12.5 for the gas-liquid simulations at increasing bubble

sizes, showing that the prediction of the cavities reflects on the prediction of the gas effect on power consumption. Data relevant to each impeller are shown in Tab.2, where the gassed/ungassed power number ratio as predicted from the torque on the impeller blades is reported.

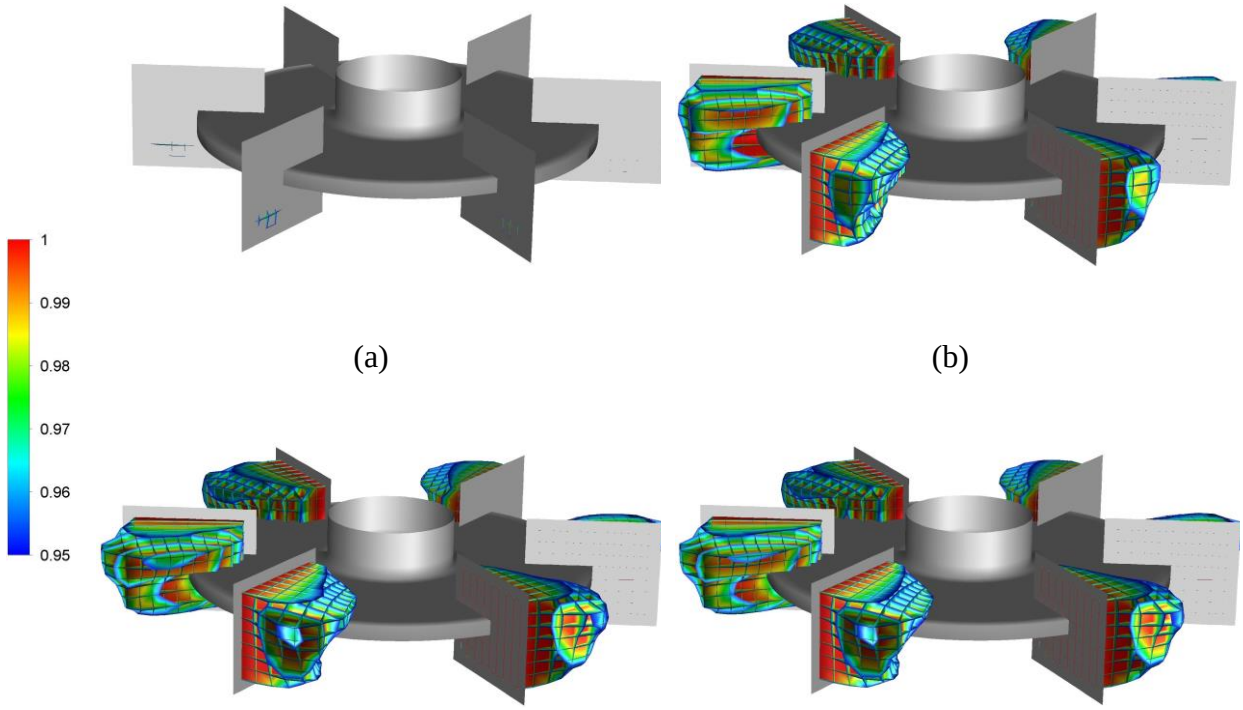

Figure 4 – Gas cavities on the lowest impeller as predicted with the simulations with constant bubble diameter of 1mm (a), 2mm (b), 3mm (c) and 4mm (d), C^{exp}=1. The color map indicates the gas volume fraction.

Table 2 – Np_g/Np_u obtained from the torque on the impeller blades as predicted with different bubble diameters

Np_g/Np_u	1mm	2mm	3mm	4mm

RT at z/T =3.5	0.93	0.86	0.66	0.66
RT at z/T =2.5	0.93	0.83	0.66	0.66
RT at z/T =1.5	0.93	0.76	0.65	0.65
RT at z/T =0.5	0.85	0.66	0.62	0.62

Tab. 2 shows that the power number decreases when the cavities form behind the impeller blades. Power numbers obtained with 3mm and 4mm bubble diameters are almost constant for the four impellers, highlighting the presence of large gas cavities behind all the impeller blades and confirming small differences between the results obtained with 3mm and 4mm bubbles, due to the equal value of the bubble terminal velocity. It is confirmed that the drop of power consumption observed in this flow regime is mainly due to the presence of the cavities, that have a bigger impact than the decrease of the gas-liquid mixture density with respect to the single liquid phase. In fact, the predicted overall gas hold-up in the tank is higher when 1mm diameter bubbles are considered, with respect to, for instance, bubbles of 2mm. Np_g in the former case is larger than in the latter, meaning that the power reduction is due to the formation of large gas cavities at the rear of the impeller blades.

The comparison of the predicted pressure field in the single phase and the gas-liquid systems provides a clear physical explanation of the power drop due to the gas cavities. As can be observed in Fig. 5, a different pressure distribution is obtained in the two cases, with similar low pressure values behind the impeller blades and a lower pressure in front of the blades for the gas-liquid with respect to the single phase case. As a result, a smaller torque and a decrease in the power drawn is observed when the gas accumulates, forming the large cavities.

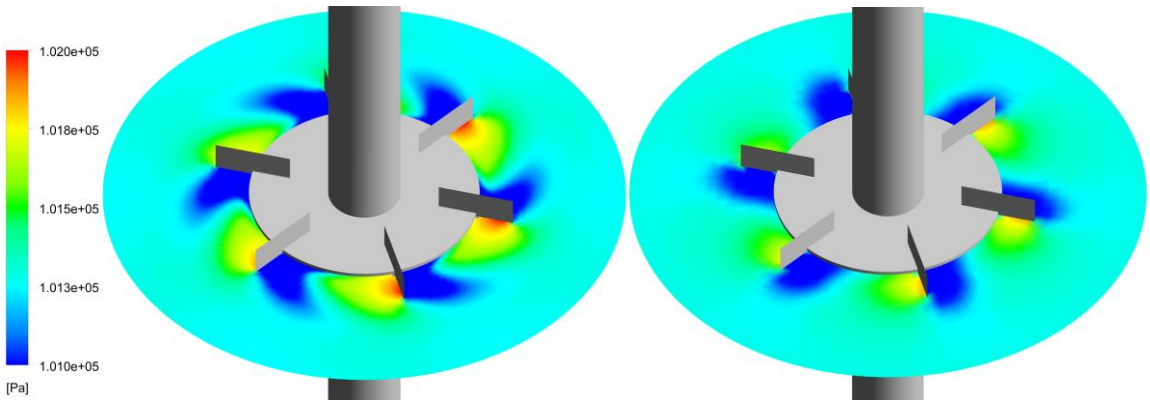

(a) (b)

Figure 5 – Map of the total pressure at z/T =0.5, 0<r/T<0.28 and N=5 s^{-1} for the stirred tank with the single phase (a) and the gas-liquid system (d_b=2mm, C^{exp}=1) (b).

The capability of the computational method to predict gassed power consumption is further confirmed by the comparison of the power reduction due to the presence of the cavities with the experimental curve obtained for a similar geometry on a single stage stirred tank [43] that is shown in Fig. 6 together with the corresponding cavity area to impeller area ratio power ratio, as a function of the gas flow number, Fl_g. As can be observed, the model reliability is also confirmed by the results obtained from an additional simulation carried out at a different gas flow rate (Q=162 L/h corresponding to a Flg =0.02).

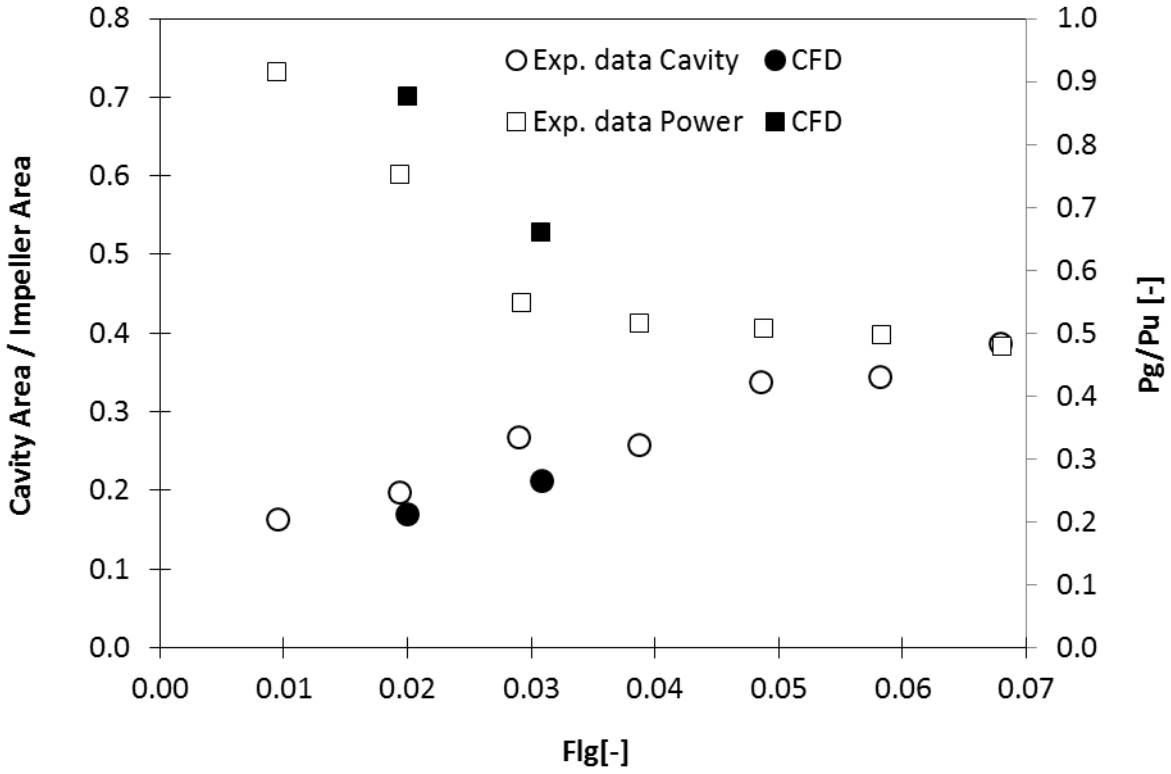

Figure 6 – Comparison between experimental (Exp.) and computational (CFD) cavity area to impeller area ratio (left y-axis) and gassed to ungassed power consumption ratio (right y-axis) as a function of the gas flow number.

The results presented in this section suggest that the selected fully predictive computational approach can capture the main fluid dynamics characteristics of the multiple impeller stirred vessel in a reliable way. Further improvement in the quantitative agreement of the simulations with the experimental values are expected with finer grids that, based on previous results on single phase systems [13], can provide more reliable turbulent variable predictions.

In the following sections, a constant diameter of 2mm was assumed since it proved successful in reproducing all the main features of the gas-liquid hydrodynamics.

5.2 Effect of the interphase forces magnitude

In this section the results obtained with the drag force and the turbulent dispersion force either considered independent (C^{exp}=0) or linearly dependent (C^{exp}=1) on the liquid phase volume fractions are discussed. Both the alternatives have been adopted in previous computational investigations of stirred tanks, without specific discussion. More frequently, the drag force reduction due to the turbulence effect [26,33,60] has been considered together with C^{exp}=0, leading to the same practical consequence on the drag force magnitude of the method selected in this work, that is the adoption of C^{exp}=1. Being the bubble diameter and shape not well defined in gas-liquid systems as opposed to solid-liquid systems, the reasoning on the drag coefficient modifications due to turbulence effects appears quite arbitrary, not only because the experimental results on the particle drag coefficient modification due to the liquid turbulence are strictly valid for very dilute systems [61], but also because the uncertainties on the bubble size identification are generally significant. As a result, it is impossible to assess whether the better agreement of the predictions accounting for the drag coefficient correction claimed in many previous works is actually affected by the choice of the bubble size.

The formation of the large gas cavities behind the lowest impeller blades with d_B=2mm was only observed when also the continuous phase volume fraction was accounted for in the formulation of the interphase forces (C^{exp}=1), whereas considering just the dispersed phase (C^{exp}=0) does not allow the formation of the cavities. This difference arises from the different force fields generated in the regions of high gas volume fraction, as can be seen in Fig. 7, where the drag force and the turbulent dispersion force fields were examined on a plane behind a blade of the lowest impeller.

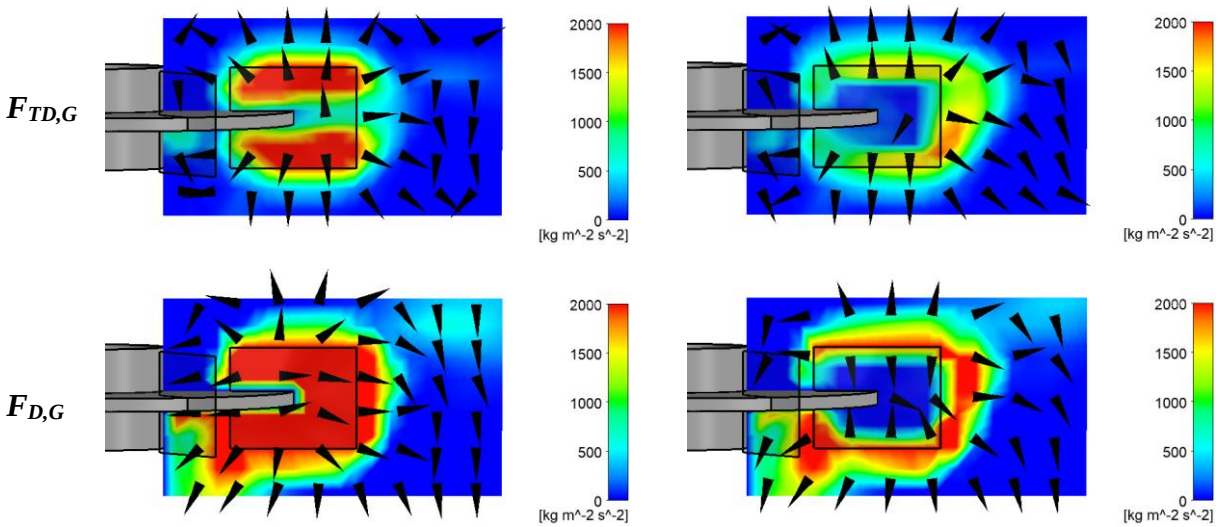

Figure 7 – Turbulent dispersion ($\mathbf{F}_{TD,G}$) and drag ($\mathbf{F}_{D,G}$) force field behind a blade of the lowest impeller. (a) C^{exp}=0; (b) C^{exp}=1. The color map indicates the magnitude of the forces and the vectors indicate their directions.

Fig. 7 shows that in the space behind the impeller blade, where gas accumulation takes place in the experimental system, including (C^{exp}=1) or not including (C^{exp}=0) the continuous phase volume fraction in Eq. 5 make a significant difference in the predicted turbulent dispersion and drag forces magnitude. For C^{exp}=0, the monotonic increase of the drag coefficient with the disperse phase volume fraction causes a monotonic increase of the forces. In this case, as can be observed in Fig. 7a along the axial edge of the blade, the drag and turbulent dispersion contributions pull the gas from the region behind the blades and prevent gas accumulation. Conversely, for C^{exp}=1, the forces are limited by the combined effect of the disperse and continuous phase volume fractions, and their reduction leads to the gas cavity prediction, as shown in Fig. 7b. Indeed, the reduced forces cannot strip the gas from the low-pressure regions, and it accumulates producing large cavities. In turn, the cavities on the impeller blades are responsible for a reduction of power transferred to the fluid,

that based on the simulations decreases by $P_g = 0.80\ P_u$, consistently with the power reduction of $P_g = 0.85 P_u$ measured in the experiments.

5.3 Mixing time

The homogenization dynamics of a passive tracer injected in the liquid phase was studied and compared with the experimental value. The injection was simulated introducing 4mL of tracer below the lowest impeller, at a position of $r/T = 0.25$ and $z/H = 0.02$. The time evolution of the tracer concentration was measured at $r/T = 0.25$ and $z/H = 0.88$. The tracer homogenization curve was obtained for the single phase (SP) operated fermenter, thus containing only the continuous liquid phase, and in two phase conditions, with bubbles of constant diameter of 1mm and 2mm and C^{exp}=1. The results are shown in Fig. 8.

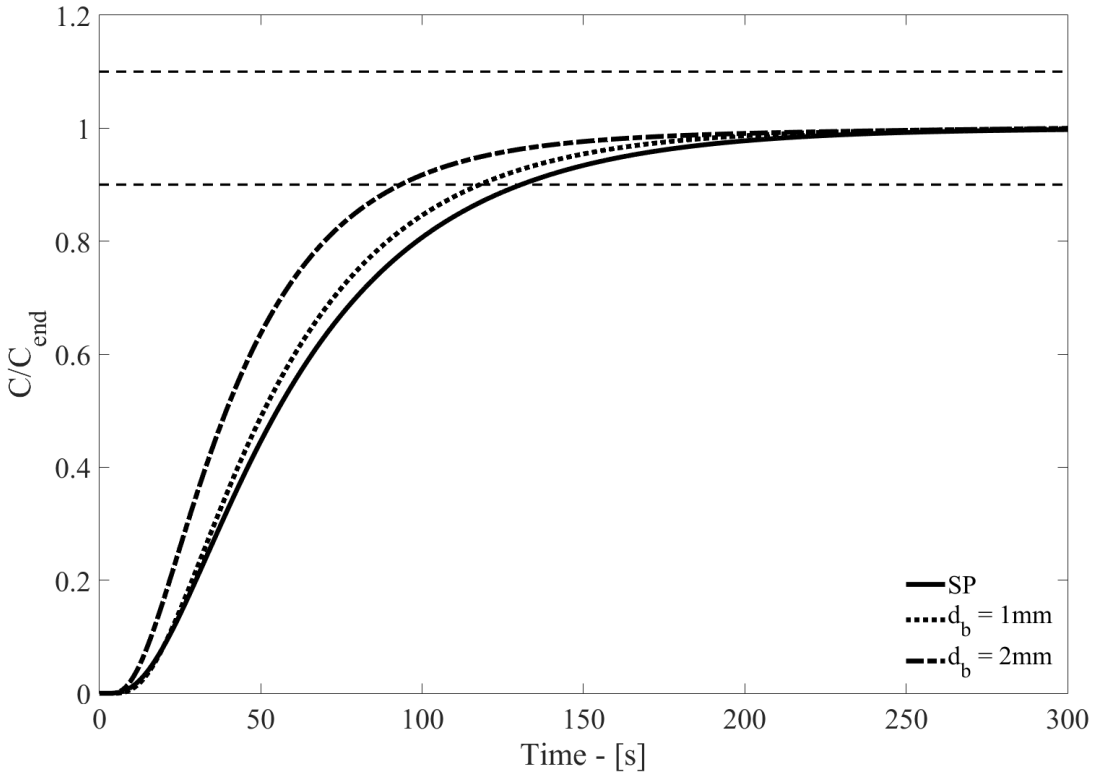

Figure 8 – Tracer homogenization curve of the single phase (SP) simulation, the gas-liquid simulations with bubble diameters of 1mm and 2mm. The dashed lines indicate a ± 10% interval with respect to the final non dimensional tracer concentration.

Qualitatively, the curves obtained from the simulations agree with the expected reduction of the mixing time due to the increased mixing action of the bubbles in two phase conditions [4]. The time needed by the tracer concentration to reach 90% of the final concentration, t_{90}, was evaluated for the three cases considered and it is reported in Tab. 3 together with the experimental value.

Table 3 – Mixing time as predicted by the experiment and by different simulations

	t_{90} [s]	Deviation from Experimental value
Experimental	68	
CFD, d_b = 1mm	118	74%
CFD, d_b = 2mm	93	37%

Fig.8 shows that significant differences are found between the single-phase simulation and the two-phase simulations, meaning that the presence of the dispersed phase considerably affects the continuous phase mixing. Moreover, in the homogenization dynamics as predicted by the two-phase simulations, substantial differences are found considering 1mm and 2mm bubbles. Bubbles with diameters of 1mm have a lower effect on the liquid flow field, resulting in a homogenization dynamic curve closer to the single-phase curve, with respect to the curve obtained with 2mm diameter bubbles.

Poor overall top-to-bottom liquid mixing, referred to as "compartmentalization", is a known issue of high aspect ratio vessels stirred with multiple impellers [59,62]. The axial dominant flow of the dispersed phase reduces the compartmentalization, fostering top-to-bottom liquid mixing and thus resulting in lower mixing times of the two-phase system with respect to the single-phase.

Finally, the t_{90} values reported in Tab. 3 show that the agreement with the experimental value of the mixing time improves with the 2mm bubbles with respect to the 1mm bubbles, but the overprediction of mixing times is still significant. The main reason is most likely due to the typical underprediction of the turbulent dissipation rate obtained with RANS based simulations, resulting in underestimated turbulent diffusivities [63]. Improvement may be expected by adopting refined

grids [13], but they were not considered in this work for the reasons already discussed in Section 4. For estimating the grid effect on the mixing time underprediction, a global correction was implemented multiplying the turbulent Schmidt number in Eq. 12 by the ratio of the numerical and experimental power number, similarly to what was done for the local turbulent variables by Gao et al. [56], resulting in a turbulent Schmidt number, Sc_t = 0.5 and a predicted t_{90} = 86s, which deviates by 26% from the experimental value. The analysis suggests that when the spatial discretization effect cannot be eliminated due to computational constrains, reasonable values of the mixing times can still be obtained by an empirical correction to the turbulent Schmidt number.

5.4 OTR and interphase mass transfer

The oxygen mass transfer from the gas phase to the liquid phase was calculated assuming a constant bubble diameter of 2mm and accounting for the effect of the liquid volume fraction on the drag calculation (C^{exp} =1), which ensure the cavity formation on the blades. The contour map of the volumetric mass transfer coefficient is reported in Fig. 9a, where the strong inhomogeneity of the k_La is apparent. Large regions with an almost nil value of the volumetric mass transfer coefficient are found below and above the lowest impeller. The volume average of the k_La as obtained from the simulation is equal to 4.3×10^{-3} 1/s (≈ 15 1/h).

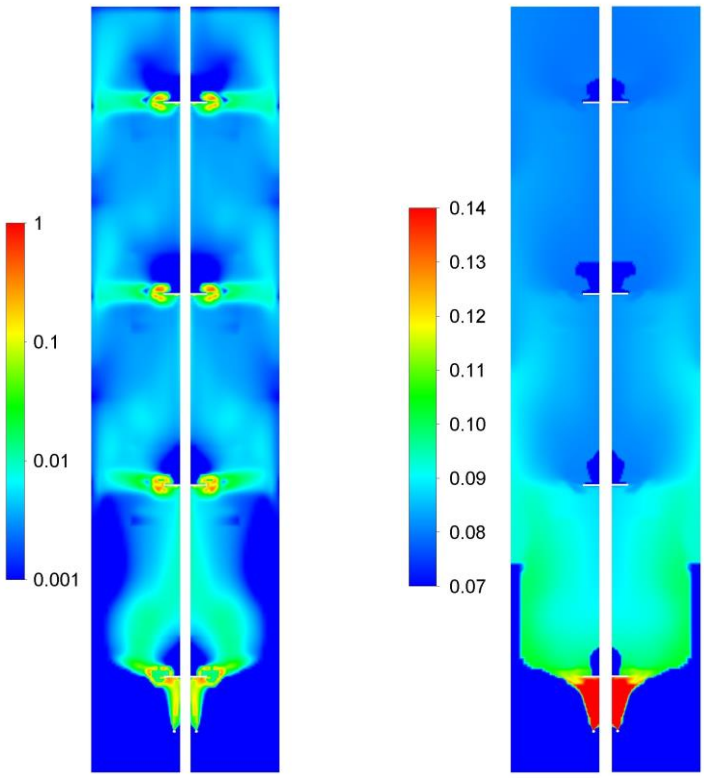

(a) (b)

Figure 9 - Volumetric mass transfer coefficient (1/s) distribution (a) and oxygen molar fraction in the gas phase (b) on a plane midway between two consecutive baffles.

It is worth observing that without the cavities, the predicted power consumption for the lowest impeller would have been overestimated by 32%, as a result, the bubble size estimated with Eq. 10 would have been 11% smaller, the gas volume fraction would have increased by 7% and according to Eq. 17, the specific interfacial area would have been 20% bigger. Finally, based on Eq. 16 the k_L would have been 7% higher, leading to an overall increase of the k_La by 28%.

To evaluate the interphase oxygen flux, a constant oxygen concentration of 3mg/L, approximately equal to 30% of the oxygen saturation in water at room temperature, was assumed in the whole fermenter volume. With dissolved oxygen concentration above 30% no oxygen

limitations are expected [64]. As soon as the dissolved oxygen exceeded that threshold, the excess oxygen mass was instantaneously removed from the liquid phase through a sink term in the species transport equation. The volume average OTR is equal to 39mmol/(Lh). The gas phase oxygen concentration distribution, reported in Fig. 9b, shows that going toward the vessel top, the mass transfer driving force is reduced. Based on the predicted local features of the OTR, improvement of the O_2 mass transport and consequently to the fermenter productivity might be obtained by geometrical or operating conditions variations performed by the numerical simulation method proposed in this work, without the recourse to pilot scale experiments.

Improvement of the fermentation performances and step forward in the fermentation intensification process are expected from the overall capability of the CFD model proposed in this work in providing detailed and reliable design and operating variables at any scale and geometry.

6 Conclusions

In this work, the turbulent two-phase fluid dynamics and the interphase oxygen transfer rate in a pilot scale fermenter stirred by multiple impellers under a typical gas-liquid flow regime adopted in industrial operations was studied through CFD simulations. A robust and reliable modelling approach in the context of the two-fluid model was identified and validated by comparison with original and literature experimental data.

In the selected operating conditions and flow regime. The results showed that the interphase interaction forces cannot increase monotonically with the disperse phase volume fraction, thus both the dispersed and continuous volume fractions must be included in the drag coefficient

calculation to predict the gas cavities and the corresponding decrease of power transferred to the system.

Purposely collected experimental data and correlations from the literature were used to validate the simulation results and the modelling approach, obtaining a good agreement on the global gas hold-up (with a maximum deviation of about 25%) and on power transferred to the gas-liquid mixture (with a maximum deviation of about 6%), provided that the fermenter hydrodynamics and the gas-liquid flow regime are correctly predicted. Better predictions of the mixing time are expected with a grid refinement, but the computational cost is not currently affordable for large-scale equipment.

Finally, the OTR was calculated, allowing the identification of regions where poor mass transfer may be responsible of a significant reduction of the potential productivity of the fermenter. Having proposed and validated a robust and reliable CFD model, future work may address the analysis of the system, the investigation of the fermenter performances and the most favourable operating conditions.

7 References

[1] A.I. Stankiewicz, J.A. Moulijn, Process intensification: Transforming chemical engineering, Chem. Eng. Prog. 96 (2000) 22–33.

[2] T. Van Gerven, A. Stankiewicz, Structure, energy, synergy, time-the fundamentals of process intensification, Ind. Eng. Chem. Res. 48 (2009) 2465–2474. https://doi.org/10.1021/ie801501y.

[3] N.M. Nikačević, A.E.M. Huesman, P.M.J. Van den Hof, A.I. Stankiewicz, Opportunities

and challenges for process control in process intensification, Chem. Eng. Process. Process Intensif. 52 (2012) 1–15. https://doi.org/10.1016/j.cep.2011.11.006.

[4] H.J. Noorman, W. Van Winden, J.J. Heijnen, R.G.J.M. Van Der Lans, Intensified Fermentation Processes and Equipment, in: RSC Green Chem., Royal Society of Chemistry, 2018: pp. 1–41. https://doi.org/10.1039/9781788010320-00001.

[5] E.H. Dunlop, S.J. Ye, Micromixing in fermentors: Metabolic changes inSaccharomyces cerevisiae and their relationship to fluid turbulence, Biotechnol. Bioeng. 36 (1990) 854–864. https://doi.org/10.1002/bit.260360816.

[6] S.O. Enfors, M. Jahic, A. Rozkov, B. Xu, M. Hecker, B. Jürgen, E. Krüger, T. Schweder, G. Hamer, D. O'Beirne, N. Noisommit-Rizzi, M. Reuss, L. Boone, C. Hewitt, C. McFarlane, A. Nienow, T. Kovacs, C. Trägårdh, L. Fuchs, J. Revstedt, P.C. Friberg, B. Hjertager, G. Blomsten, H. Skogman, S. Hjort, F. Hoeks, H.Y. Lin, P. Neubauer, R. van der Lans, K. Luyben, P. Vrabel, A. Manelius, Physiological responses to mixing in large scale bioreactors., J. Biotechnol. 85 (2001) 175–85. https://doi.org/10.1016/S0168-1656(00)00365-5.

[7] F. Maluta, M. Pigou, G. Montante, J. Morchain, Modeling the effects of substrate fluctuations on the maintenance rate in bioreactors with a probabilistic approach, Biochem. Eng. J. (2020) 107536. https://doi.org/10.1016/j.bej.2020.107536.

[8] R. Takors, Scale-up of microbial processes: Impacts, tools and open questions, J. Biotechnol. 160 (2012) 3–9. https://doi.org/10.1016/j.jbiotec.2011.12.010.

[9] H.J. Noorman, J.J. Heijnen, Biochemical engineering's grand adventure, Chem. Eng. Sci. 170 (2017) 677–693. https://doi.org/10.1016/j.ces.2016.12.065.

[10] C. Haringa, A.T. Deshmukh, R.F. Mudde, H.J. Noorman, Euler-Lagrange analysis towards representative down-scaling of a 22 m 3 aerobic S. cerevisiae fermentation, Chem. Eng. Sci. 170 (2017) 653–669. https://doi.org/10.1016/j.ces.2017.01.014.

[11] P. Neubauer, S. Junne, Scale-down simulators for metabolic analysis of large-scale bioprocesses, Curr. Opin. Biotechnol. 21 (2010) 114–121. https://doi.org/10.1016/j.copbio.2010.02.001.

[12] C. Haringa, R.F. Mudde, H.J. Noorman, From industrial fermentor to CFD-guided downscaling: what have we learned?, Biochem. Eng. J. 140 (2018) 57–71. https://doi.org/10.1016/j.bej.2018.09.001.

[13] M. Coroneo, G. Montante, A. Paglianti, F. Magelli, CFD prediction of fluid flow and mixing in stirred tanks: Numerical issues about the RANS simulations, Comput. Chem. Eng. 35 (2011) 1959–1968. https://doi.org/10.1016/j.compchemeng.2010.12.007.

[14] M.M.C.G. Warmoeskerken, J.M. Smith, Flooding of disc turbines in gas-liquid dispersions: A new description of the phenomenon, Chem. Eng. Sci. 40 (1985) 2063–2071. https://doi.org/10.1016/0009-2509(85)87023-8.

[15] K.M. Gezork, W. Bujalski, M. Cooke, A.W. Nienow, Mass Transfer and Hold-up Characteristics in a Gassed, Stirred Vessel at Intensified Operating Conditions, Chem. Eng. Res. Des. 79 (2001) 965–972. https://doi.org/10.1205/02638760152721514.

[16] L. Niño, R. Gelves, H. Ali, J. Solsvik, H. Jakobsen, Applicability of a modified breakage and coalescence model based on the complete turbulence spectrum concept for CFD simulation of gas-liquid mass transfer in a stirred tank reactor, Chem. Eng. Sci. 211 (2020) 115272. https://doi.org/10.1016/j.ces.2019.115272.

[17] A.W. Nienow, M.D. Lilly, Power drawn by multiple impellers in sparged agitated vessels, Biotechnol. Bioeng. 21 (1979) 2341–2345.

[18] H. Ameur, 3D hydrodynamics involving multiple eccentric impellers in unbaffled cylindrical tank, Chinese J. Chem. Eng. 24 (2016) 572–580. https://doi.org/10.1016/j.cjche.2015.12.010.

[19] H. Ameur, M. Bouzit, A. Ghenaim, Numerical study of the performance of multistage Scaba 6SRGT impellers for the agitation of yield stress fluids in cylindrical tanks, J. Hydrodyn. 27 (2015) 436–442. https://doi.org/10.1016/S1001-6058(15)60501-7.

[20] N.G. Deen, T. Solberg, B.H. Hjertager, Flow Generated by an Aerated Rushton Impeller: Two-phase PIV Experiments and Numerical Simulations, Can. J. Chem. Eng. 80 (2002) 1–15. https://doi.org/10.1002/cjce.5450800406.

[21] A. Khopkar, J. Aubin, C. Rubio-Atoche, C. Xuereb, N. Le Sauze, J. Bertrand, V. V. Ranade, Flow Generated by Radial Flow Impellers: PIV Measurements and CFD Simulations, Int. J. Chem. React. Eng. 2 (2004). https://doi.org/10.2202/1542-6580.1146.

[22] A.R. Khopkar, A.R. Rammohan, V.V. Ranade, M.P. Dudukovic, Gas–liquid flow generated by a Rushton turbine in stirred vessel: CARPT/CT measurements and CFD simulations, Chem. Eng. Sci. 60 (2005) 2215–2229. https://doi.org/10.1016/j.ces.2004.11.044.

[23] F. Kerdouss, A. Bannari, P. Proulx, CFD modeling of gas dispersion and bubble size in a double turbine stirred tank, Chem. Eng. Sci. 61 (2006) 3313–3322. https://doi.org/10.1016/j.ces.2005.11.061.

[24] S.S. Kshatriya, A.W. Patwardhan, A. Eaglesham, Experimental and CFD Characterization of Gas Dispersing Asymmetric Parabolic Blade Impellers, Int. J. Chem. React. Eng. 5

(2007). https://doi.org/10.2202/1542-6580.1381.

[25] F. Scargiali, A. D'Orazio, F. Grisafi, A. Brucato, Modelling and Simulation of Gas–Liquid Hydrodynamics in Mechanically Stirred Tanks, Chem. Eng. Res. Des. 85 (2007) 637–646. https://doi.org/10.1205/cherd06243.

[26] G.L. Lane, M.P. Schwarz, G.M. Evans, Numerical modelling of gas–liquid flow in stirred tanks, Chem. Eng. Sci. 60 (2005) 2203–2214. https://doi.org/10.1016/j.ces.2004.11.046.

[27] A.R. Khopkar, V. V. Ranade, CFD simulation of gas–liquid stirred vessel: VC, S33, and L33 flow regimes, AIChE J. 52 (2006) 1654–1672. https://doi.org/10.1002/aic.10762.

[28] G. Montante, D. Horn, A. Paglianti, Gas–liquid flow and bubble size distribution in stirred tanks, Chem. Eng. Sci. 63 (2008) 2107–2118. https://doi.org/10.1016/j.ces.2008.01.005.

[29] P. Shi, R. Rzehak, Bubbly flow in stirred tanks: Euler-Euler/RANS modeling, Chem. Eng. Sci. 190 (2018) 419–435. https://doi.org/10.1016/j.ces.2018.06.001.

[30] A. Buffo, M. Vanni, D.L. Marchisio, Multidimensional population balance model for the simulation of turbulent gas–liquid systems in stirred tank reactors, Chem. Eng. Sci. 70 (2012) 31–44. https://doi.org/10.1016/j.ces.2011.04.042.

[31] M. Jahoda, L. Tomášková, M. Moštěk, CFD prediction of liquid homogenisation in a gas–liquid stirred tank, Chem. Eng. Res. Des. 87 (2009) 460–467. https://doi.org/10.1016/j.cherd.2008.12.006.

[32] J. Gimbun, C.D. Rielly, Z.K. Nagy, Modelling of mass transfer in gas–liquid stirred tanks agitated by Rushton turbine and CD-6 impeller: A scale-up study, Chem. Eng. Res. Des. 87 (2009) 437–451. https://doi.org/10.1016/j.cherd.2008.12.017.

[33] A.R. Khopkar, P.A. Tanguy, CFD simulation of gas–liquid flows in stirred vessel equipped

with dual rushton turbines: influence of parallel, merging and diverging flow configurations, Chem. Eng. Sci. 63 (2008) 3810–3820. https://doi.org/10.1016/j.ces.2008.04.039.

[34] A.R. Khopkar, G.R. Kasat, A.B. Pandit, V.V. Ranade, CFD simulation of mixing in tall gas–liquid stirred vessel: Role of local flow patterns, Chem. Eng. Sci. 61 (2006) 2921–2929. https://doi.org/10.1016/j.ces.2005.09.023.

[35] M. Taghavi, R. Zadghaffari, J. Moghaddas, Y. Moghaddas, Experimental and CFD investigation of power consumption in a dual Rushton turbine stirred tank, Chem. Eng. Res. Des. 89 (2011) 280–290. https://doi.org/10.1016/j.cherd.2010.07.006.

[36] D. Fajner, D. Pinelli, R.S. Ghadge, G. Montante, A. Paglianti, F. Magelli, Solids distribution and rising velocity of buoyant solid particles in a vessel stirred with multiple impellers, Chem. Eng. Sci. 63 (2008) 5876–5882. https://doi.org/10.1016/j.ces.2008.08.033.

[37] S.U. Ahmed, P. Ranganathan, A. Pandey, S. Sivaraman, Computational fluid dynamics modeling of gas dispersion in multi impeller bioreactor, J. Biosci. Bioeng. 109 (2010) 588–597. https://doi.org/10.1016/j.jbiosc.2009.11.014.

[38] Y. Liu, Z.-J. Wang, J. Xia, C. Haringa, Y. Liu, J. Chu, Y.-P. Zhuang, S.-L. Zhang, Application of Euler-Lagrange CFD for quantitative evaluating the effect of shear force on Carthamus tinctorius L. cell in a stirred tank bioreactor, Biochem. Eng. J. 114 (2016) 209–217. https://doi.org/10.1016/j.bej.2016.07.006.

[39] H. Wang, X. Jia, X. Wang, Z. Zhou, J. Wen, J. Zhang, CFD modeling of hydrodynamic characteristics of a gas–liquid two-phase stirred tank, Appl. Math. Model. 38 (2014) 63–92. https://doi.org/10.1016/j.apm.2013.05.032.

[40] S.M. Teli, V.S. Pawar, C. Mathpati, Experimental and Computational Studies of Aerated

Stirred Tank with Dual Impeller, Int. J. Chem. React. Eng. 18 (2020). https://doi.org/10.1515/ijcre-2019-0172.

[41] G.K. Gakingo, K.G. Clarke, T.M. Louw, A numerical investigation of the hydrodynamics and mass transfer in a three-phase gas-liquid-liquid stirred tank reactor, Biochem. Eng. J. 157 (2020) 107522. https://doi.org/10.1016/j.bej.2020.107522.

[42] A.W. Nienow, M.M.C.G. Warmoeskerken, J.M. Smith, M. Konno, On the flooding/loading transition and the complete dispersal condition in aerated vessels agitated by a Rushton-turbine, in: Proc. 5th Eur. Conf. Mix., BHRA Fluid Engineering, Wurzburg, Germany, 1985: pp. 143–154.

[43] A. Paglianti, M. Fujasova, G. Montante, A simple model for power consumption in gassed and boiling stirred vessels, AIChE J. 54 (2008) 646–656. https://doi.org/10.1002/aic.11414.

[44] ANSYS Inc., ANSYS Fluent Theory Guide R19 vol. 2, 19th ed., Canonsburg, PA, 2016.

[45] A.D. Burns, T. Frank, I. Hamill, J.-M.M. Shi, The Favre Averaged Drag Model for Turbulent Dispersion in Eulerian Multi-Phase Flows, in: Fifth Int. Conf. Multiph. Flow, ICMF-2004, Yokohama, Japan, 2004: pp. 1–17.

[46] R. Clift, J.R. Grace, M.E. Weber, Bubbles, drops, and particles, 1st ed., Dover Publications, Inc., Mineola, New York, 2005.

[47] L. Schiller, A. Naumann, Über die grundlegenden berechnungen bei der schwerkraftbereitung, Zeitschrift Des Vereines Dtsch. Fngenieure. 77 (1933) 318--321.

[48] D.F. Fletcher, D.D. McClure, J.M. Kavanagh, G.W. Barton, CFD simulation of industrial bubble columns: Numerical challenges and model validation successes, Appl. Math. Model. 44 (2017) 25–42. https://doi.org/10.1016/j.apm.2016.08.033.

[49] D.D. McClure, H. Norris, J.M. Kavanagh, D.F. Fletcher, G.W. Barton, Validation of a Computationally Efficient Computational Fluid Dynamics (CFD) Model for Industrial Bubble Column Bioreactors, Ind. Eng. Chem. Res. 53 (2014) 14526–14543. https://doi.org/10.1021/ie501105m.

[50] D.D. McClure, J.M. Kavanagh, D.F. Fletcher, G.W. Barton, Development of a CFD Model of Bubble Column Bioreactors: Part Two - Comparison of Experimental Data and CFD Predictions, Chem. Eng. Technol. 37 (2014) 131–140. https://doi.org/10.1002/ceat.201300546.

[51] S.S. Alves, C.I. Maia, J.M.T. Vasconcelos, A.J. Serralheiro, Bubble size in aerated stirred tanks, Chem. Eng. J. 89 (2002) 109–117. https://doi.org/10.1016/S1385-8947(02)00008-6.

[52] Wang, Z.-S. Mao, C. Yang, Experimental and Numerical Investigation on Gas Holdup and Flooding in an Aerated Stirred Tank with Rushton Impeller, Ind. Eng. Chem. Res. 45 (2006) 1141–1151. https://doi.org/10.1021/ie0503085.

[53] Y. Zhang, C. Yang, Z. Mao, Large eddy simulation of the gas–liquid flow in a stirred tank, AIChE J. 54 (2008) 1963–1974. https://doi.org/10.1002/aic.11516.

[54] J.C. Lamont, D.S. Scott, An eddy cell model of mass transfer into the surface of a turbulent liquid, AIChE J. 16 (1970) 513–519. https://doi.org/10.1002/aic.690160403.

[55] F. Maluta, A. Paglianti, G. Montante, Modelling of biohydrogen production in stirred fermenters by Computational Fluid Dynamics, Process Saf. Environ. Prot. 125 (2019) 342–357. https://doi.org/10.1016/j.psep.2018.09.020.

[56] Z. Gao, D. Li, A. Buffo, W. Podgórska, D.L. Marchisio, Simulation of droplet breakage in turbulent liquid–liquid dispersions with CFD-PBM: Comparison of breakage kernels,

Chem. Eng. Sci. 142 (2016) 277–288. https://doi.org/10.1016/j.ces.2015.11.040.

[57] H.. Versteeg, W. Malalasekera, An Introduction to Computational Fluid Dynamics - The Finite Volume Method, 2nd ed., Pearson Education Limited, Harlow, England (UK), 2007.

[58] J.C. Middleton, Gas-liquid dispersion and mixing, in: A.W. Nienow, M.F. Edwards, N. Harnby (Eds.), Mix. Process Ind., Butterworth-Heinemann, London, 1997: pp. 322–363.

[59] J.C. Middleton, J.M. Smith, Gas-liquid mixing in turbulent systems, in: E.L. Paul, V.A. Atiemo-Obeng, S.M. Kresta (Eds.), Handb. Ind. Mix. Sci. Pract., John Wiley & Sons Inc., Hoboken, New Jersey, 2004: pp. 585–638.

[60] A. Bakker, H.E.A. Van den Akker, Computational model for the gas-liquid flow in stirred reactors, Chem. Eng. Res. Des. 72 (1994) 594–606.

[61] A. Brucato, F. Grisafi, G. Montante, Particle drag coefficients in turbulent fluids, Chem. Eng. Sci. 53 (1998) 3295–3314. https://doi.org/10.1016/S0009-2509(98)00114-6.

[62] F. Magelli, G. Montante, D. Pinelli, A. Paglianti, Mixing time in high aspect ratio vessels stirred with multiple impellers, Chem. Eng. Sci. 101 (2013) 712–720. https://doi.org/10.1016/j.ces.2013.07.022.

[63] G. Montante, F. Magelli, Liquid Homogenization Characteristics in Vessels Stirred with Multiple Rushton Turbines Mounted at Different Spacings, Chem. Eng. Res. Des. 82 (2004) 1179–1187. https://doi.org/10.1205/cerd.82.9.1179.44163.

[64] G. Larsson, M. Tornkvist, E.S. Wernersson, C. Tragaardh, H. Noorman, S.O. Enfors, Substrate gradients in bioreactors: origin and consequences, Bioprocess Eng. 14 (1996) 281–289. https://doi.org/10.1007/BF00369471.